Quantum Electronics **35** (5) 454 – 466 (2005)

INTERACTION OF LASER RADIATION WITH MATTER. LASER PLASMA

PACS numbers: 52.38.Mf
DOI: 10.1070/QE2005v035n05ABEH002783

Plasma-mediated surface evaporation of an aluminium target in vacuum under UV laser irradiation

V.I. Mazhukin, V.V. Nosov

Abstract. **Mathematical simulation is employed to investigate the dynamics of evaporation and condensation on the surface of a metal target under the conditions of plasma production in the vaporised material exposed to the 0.248-μm UV radiation of a KrF laser with the intensity $G_0 = 2 \times 10^8 - 10^9$ W cm^{-2}, and a pulse duration $\tau = 20$ ns. A transient two-dimensional mathematical model is used, which includes, for the condensed medium, the heat conduction equation with the Stefan boundary condition and additional kinetic conditions at the evaporation surface and, for the vapour, the equations of radiative gas dynamics and laser radiation transfer supplemented with tabular data for the parameters of the equations of state and absorption coefficients. The target evaporation in vacuum induced by the UV radiation was found to occur during the laser pulse and is divided into two characteristic stages: initial evaporation with a sound velocity and subsonic evaporation after the plasma production. At the subsonic evaporation stage, one part of the laser radiation passes through the plasma and is absorbed by the target surface and another part is absorbed in a thin plasma layer near the surface to produce a high pressure, which significantly moderates the vapour ejection. After completion of the pulse, a part of the vaporised material is condensed on the surface, both in the evaporation region and some distance away from it due to the lateral expansion of the plasma cloud.**

Keywords: *surface evaporation, Mach number, laser plasma, radiative gas dynamics.*

1. Introduction

The evaporation of materials by intense radiation is qualitatively different in character depending on the temperature and pressure in the surface region. When the temperature and (or) the pressure exceed critical values, the liquid – vapour transition is described by gas-dynamic equations with a continuous equation of state [1]. In the opposite (subcritical) case, the process is characterised by the formation of a sharp phase boundary. The vaporised material flow is nonequilibrium, because the velocities of all particles are initially directed away from the surface. When the evaporation is intense enough, the particles collide with the formation of a reverse flow, and an equilibrium distribution is established at distances equal to several path lengths. The region where the equilibrium sets in is referred to as the Knudsen layer (KL).

For the equations of continuum mechanics, a thin KL is a region with a strong discontinuity of gas-dynamic parameters [2 – 6], which obeys the mass, momentum, and energy flux conservation laws and some additional relationships that take into account the kinetics of the phase transition. They can be obtained with the help of different approximations of the in-layer distribution function [2 – 4, 7, 8] or solving the boundary-value problem for the Boltzmann equation in the half-space filled with vapour and bounded by the surface of the condensed medium [9, 10]. In the latter case, the values of macroscopic parameters established at infinity will correspond to the vapour at the outer side of the KL, while the values at the boundary – to the condensed medium.

Evaporation and condensation are not symmetric processes, which is reflected in the formulation of the boundary conditions at the interface between the condensed medium and the vapour. In the case of evaporation, the three parameters which characterise the vapour – the temperature, the density (or the pressure), and the velocity – are related by two equations. In this case, the degree of nonequilibrium (the intensity) of the process is conveniently characterised by the Mach number on the outside of the KL. The condition $M = 0$ implies that the total material flux through the boundary is equal to zero and the vapour is in equilibrium. Positive values of M correspond to evaporation, which can take place in two qualitatively different regimes. Upon evaporation with a sound velocity, when $M = 1$, the material flux through the interface is highest, the process takes place under strongest nonequilibrium, and the behaviour of condensed medium is independent of the state of the vapour region. This regime is realised when the target is exposed to laser radiation with a constant intensity in vacuum or in a medium with a low counterpressure [11]. Upon subsonic evaporation ($0 < M < 1$), the description of the effect becomes more complicated, because the processes in the condensed and gaseous media turn out to be interrelated, while the value of M for the boundary conditions is unknown and should be determined during the solution of the problem [12]. It is commonly assumed that the gas-dynamic vapour velocity does not exceed the

V.I. Mazhukin, V.V. Nosov Institute of Mathematical Modelling, Russian Academy of Sciences, Miusskaya pl. 4a, 125047 Moscow, Russia; e-mail: immras@orc.ru, nosov@orc.ru

Received 1 March 2005
Kvantovaya Elektronika **35** (5) 454 – 466 (2005)
Translated by E.N. Ragozin

local sound velocity, and the regimes with $M > 1$ are not considered [2–4, 7–13].

Negative Mach numbers correspond to the process of surface condensation, which occurs when the pressure of the gaseous medium exceeds the saturated vapour pressure. In the regime of subsonic condensation, when $-1 < M < 0$, the three quantities which characterise the vapour (temperature, density, and velocity), according to Ref. [10] are related by one additional equation. When the flow velocity on the outer boundary of the KL becomes supersonic ($M < -1$), the relationship between the admissible values of the parameters takes on the form of an inequality.

Transient laser evaporation regimes were investigated in several theoretical papers [14–21]. It was found that the factors responsible for the decrease of the Mach number at the evaporation surface are the counterpressure of an external gaseous medium [17–19], the rapid change in the temperature of the irradiated surface, when evaporation may be moderated due to the reaction of previously vaporised material [20, 21], and the additional counterpressure appearing due to a strong absorption of laser radiation in the erosion plasma [15, 16].

The emergence of laser plasma near the irradiated surface significantly complicates the general character of the action due to a sharp change in the optical and thermal properties of the vaporised material, which in turn leads to a change in the spatiotemporal energy distribution. Numerical investigations of laser evaporation and the dynamics of vapour plasma were earlier reported in several papers within the framework of spatially one-dimensional [22–24] and two-dimensional [25–28] formulation of the problem. However, the simplified treatment of evaporation in the presence of counterpressure did not permit the authors of Refs [22–28] to obtain in the explicit form the dependence of the degree of nonequilibrium of the phase transition on the pressure in the plasma, although the screening action of the laser plasma was pointed out in the majority of papers.

By using a more correct formulation of the problem in a spatially one-dimensional approximation, the authors of papers [15, 16] established the decisive role of gas-dynamic effect of the laser plasma on evaporation. The plasma production resulted not only in a decrease in the vaporised material flow, but also changed the direction of the phase transition. Due to a high plasma pressure, which was much higher than the saturated vapour pressure, the condensation on the irradiated surface began despite the fact that the surface temperature of the condensed medium was 1.5–2 times higher than the temperature of equilibrium boiling under normal conditions. Calculations showed that evaporation proceeded in two stages: the first stage was caused by the action of laser radiation ($M = 1$) and the second by intrinsic plasma radiation flux ($M \approx 0.1$).

In a more complex two-dimensional formulation of the problem, when the surface evaporation is determined by the temperature and pressure distributions in the focal spot region, the problem of the gas-dynamic effect of laser plasma on evaporation remained unexplored. Its solution will allow determining the spatiotemporal structure of vaporised material flux, its change and interrelation with the evolution of the laser plasma. Analysis of these issues is also of significance to several technological applications based on laser ablation such as film deposition, surface processing, and cluster production [29, 30].

The aim of our work is to investigate, in the two-dimensional formulation of the problem, the dynamics of material evaporation and condensation on the surface of an aluminium target and their interrelation with the dynamics of the laser plasma produced in the vaporised material exposed to the 0.248-μm UV radiation from a KrF laser emitting 20-ns pulses with the peak intensity $G_0 = 2\times 10^8 - 10^9$ W cm^{-2}.

2. Physicomathematical model

Pulsed laser irradiation of a metal target in vacuum is accompanied by several processes related to absorption and reflection of the laser radiation, the heating, melting, and evaporation of the target, and also to the gas-dynamic vapour expansion and the production of laser plasma in the vaporised material. In the general case, this problem should be solved by considering the melt motion. However, upon irradiation by short pulses with a relatively high intensity, the description of the processes may be substantially simplified. To do this, the following processes were excluded from consideration:

– the target melting, which has a weak effect on the total energy balance in the regime of developed evaporation because the latent heat of melting is much smaller than the evaporation heat;

– the hydrodynamic melt motion, which has only an insignificant effect on the total picture of processes in the nanosecond irradiation range but substantially complicates the model of the condensed medium and the computational algorithm.

In addition, we assumed that the laser plasma was in the state of local thermodynamic equilibrium, its motion was described in the nonviscous non-heat-conducting gas approximation, and the evaporation rate in vacuum was limited by the sound velocity ($M \leqslant 1$).

As a result, we obtained a mathematical model including the heat conduction equation for a condensed medium with the Stefan boundary condition and additional kinetic conditions at the evaporating surface. For the gaseous medium (the vapour), we used the model of radiative gas dynamics with the equation of laser radiation transfer supplemented with the equations of state and absorption coefficients written in a table form.

These processes were mathematically described in a mobile cylindrical coordinate system co-moving with the surface. Its origin coincided with the centre of the laser beam, the r axis was directed along the surface, and the z axis was directed along the external normal to the surface towards laser radiation (Fig. 1).

2.1 Condensed medium

In the region $0 < r < L_r$, $-l_z < z < 0$ occupied by a condensed medium (Fig. 1), the heat transfer is described by the heat conduction equation [31]

$$\rho_c c_p \left(\frac{\partial T_c}{\partial t} + V_c \frac{\partial T_c}{\partial z}\right) = \frac{1}{r}\frac{\partial}{\partial r}\left(r\Lambda_c \frac{\partial T_c}{\partial r}\right) + \frac{\partial}{\partial z}\left(\Lambda_c \frac{\partial T_c}{\partial z}\right), \quad (1)$$

where the subscript 'c' denotes the condensed medium; T_c is the temperature; V_c is the velocity of the evaporation (condensation) front; ρ_c, c_p, Λ_c are the density, specific heat, and heat conduction. The external boundaries of the region are assumed to be thermally insulated, the symmetry

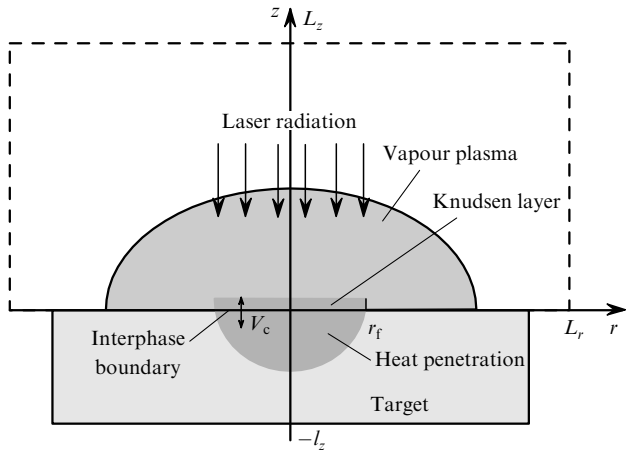

Figure 1. Scheme illustrating the laser radiation – target interaction.

condition is fulfilled at the boundary $r = 0$, and the initial target temperature is $T_0 = 300$ K.

2.2 Gaseous medium and plasma

Processes in vapour in the region $0 < (r \times z) < (L_r \times L_z)$ were described by using the system of radiative gas-dynamics equations and the laser-radiation transfer equation [32]:

$$\frac{\partial \rho}{\partial t} + \frac{1}{r}\frac{\partial}{\partial r}(r\rho u) + \frac{\partial}{\partial z}(\rho v) = 0, \tag{2}$$

$$\frac{\partial}{\partial t}(\rho u) + \frac{1}{r}\frac{\partial}{\partial r}(r\rho u^2) + \frac{\partial}{\partial z}(\rho uv) = -\frac{\partial p}{\partial r}, \tag{3}$$

$$\frac{\partial}{\partial t}(\rho v) + \frac{1}{r}\frac{\partial}{\partial r}(r\rho uv) + \frac{\partial}{\partial z}(\rho v^2) = -\frac{\partial p}{\partial z}, \tag{4}$$

$$\frac{\partial}{\partial t}(\rho e) + \frac{1}{r}\frac{\partial}{\partial r}(r\rho ue) + \frac{\partial}{\partial z}(\rho ve) = -p\left[\frac{1}{r}\frac{\partial}{\partial r}(ru) + \frac{\partial v}{\partial z}\right] - \frac{1}{r}\frac{\partial q_r}{\partial r} - \frac{\partial q_z}{\partial z} + \frac{\partial G}{\partial z}, \tag{5}$$

$$\operatorname{div} \boldsymbol{q}_v + c\kappa_v U_v = c\kappa_v U_{v\mathrm{eq}}, \quad \boldsymbol{q}_v = -\frac{c}{3\kappa_v}\operatorname{grad} U_v, \tag{6}$$

$$U_{v\mathrm{eq}} = \frac{8\pi h v^3}{c^3\{\exp[hv/(kT)] - 1\}},$$

$$\frac{\partial G^-}{\partial z} - \kappa G^- = 0, \quad \frac{\partial G^+}{\partial z} + \kappa G^+ = 0,$$

$$G = G^- - G^+, \quad 0 < z < L_z, \quad 0 < r < 2r_f, \tag{7}$$

$$p = p(\rho, T), \tag{8}$$

$$e = e(\rho, T), \tag{9}$$

$$\kappa_v = \kappa_v(\rho, T, v), \tag{10}$$

where u and v are the components of the vapour velocity vector; ρ, p and e are the density, the pressure, and the volume density of internal vapour energy; $\boldsymbol{q} = (q_r, q_z) = \int_v \boldsymbol{q}_v \mathrm{d}v$ is the plasma radiative energy flux; κ_v is the spectral absorption coefficient; U_v and $U_{v\mathrm{eq}}$ are the spectral and equilibrium plasma radiation densities; and r_f is the laser beam radius. Equations (6) describe the radiative transfer in the diffusion approximation [32, 33]. The laser-radiation transfer equation (7) takes into account both z-components of radiation intensity, the component incident on the target surface (G^-) and the reflected one (G^+). The tabulated equations of state (8), (9) were borrowed from Ref. [34]. Absorption coefficients (10) were calculated by using the Hartree – Fock – Slater model [35]. The results of calculations were presented in the form of 3D tables. The charge composition of the plasma and the excited-state distribution were determined from the Saha – Boltzmann equations [33].

The absorption coefficient $\kappa = \kappa(T, \rho)$ for the 0.248-μm ($hv \approx 5$ eV) laser radiation was determined in the same way as the coefficient κ_v [35]. Its magnitude is determined by the total contribution of free – free (the inverse bremsstrahlung effect) and bound – free transitions (photoionisation) [36]. Figure 2 shows the dependence $\kappa(T)$ and the temperature dependence of the inverse bremsstrahlung coefficient $\kappa_b(T)$ for two values of the density ρ. It follows from Fig. 2 that the total absorption coefficients have nonmonotonic temperature dependences. For $\rho = 10^{-3}$ g cm^{-3} [curve (*1*)], the coefficient κ rapidly increases in the region $T < 0.9$ eV. In this case, the dominant part is played by the photoionisation of excited states of neutral atoms, which are populated at the characteristic temperature $T \approx (0.1 - 0.2)E_{ex}$, where $E_{ex} \approx 3 - 6$ eV is the energy of excited states of neutral aluminium atoms [33, 35]. As the temperature further increases ($T > 1$ eV), the coefficient begins to decrease, and in the range of temperatures comparable with the ground-state ionisation potential of atomic aluminium ($T > 5$ eV) it is almost entirely determined by the inverse bremsstrahlung effect. At a higher density ($\rho = 5 \times 10^{-2}$ g cm^{-3}) we obtain a similar temperature dependence of the absorption coefficient, but maximum is achieved at a higher temperature ($T \approx 2$ eV).

The system of equations (2) – (10) was supplemented with the following initial and boundary conditions:

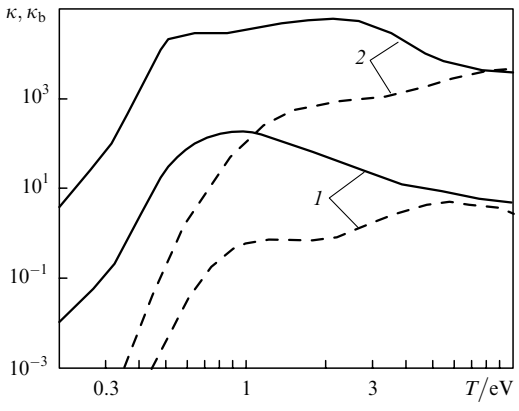

Figure 2. Temperature dependences of the tabulated absorption coefficients κ for the 0.248-μm radiation (solid curves) and the inverse bremsstrahlung coefficients (dashed curves) for the densities $\rho = 10^{-3}$ (*1*) и 5×10^{-2} g cm^{-3} (*2*).

for $t = t_0$,

$$u = v = 0, \quad T = T_0, \quad \rho = \rho_0, \quad 0 \leqslant (r \times z) \leqslant (L_r \times L_z), \tag{11}$$

for $r = 0$

$$u = 0, \quad \frac{\partial \rho}{\partial r} = \frac{\partial v}{\partial r} = \frac{\partial p}{\partial r} = 0, \quad q_r = 0, \tag{12}$$

for $r = L_r$

$$p = p_0, \quad \rho = \rho_0, \quad u = v = 0, \quad q_r = -cU_v/2, \tag{13}$$

for $z = L_z$

$$p = p_0, \quad \rho = \rho_0, \quad u = v = 0, \quad q_z = -cU_v/2, \tag{14}$$

$$G^- \equiv G_0 \exp[-(r/r_f)^2] \exp[-4(t/\tau - 1)^2], \quad 0 < r < 2r_f,$$

for $z = 0$

$$G^+ = [1 - A(T)]G^-, \quad 0 < r < 2r_f, \tag{15}$$

where τ is the laser pulse duration and $A(T)$ is the surface absorptivity. The background density ρ_0 was assumed to be equal to 3×10^{-6} g cm^{-3} ($p_0 = 2 \times 10^{-3}$ bar).

2.3 Interphase boundary conditions

The boundary conditions at the target surface relate six quantities: the velocity V_c, the temperature T_c, and the pressure p_c at the surface, the temperature T, the density ρ, and the normal vapour velocity component v at the exterior boundary of the KL. Independently of the direction of the phase transition, they obey three conservation laws: for energy, mass, and momentum:

$$\Lambda_c \frac{\partial T_c}{\partial z} = AG^- + L_v \rho_c V_c, \quad \rho_c V_c = \rho(V_c - v),$$

$$\rho_c V_c^2 + p_c = \rho(V_c - v)^2 + p, \tag{16}$$

where L_v is the heat of evaporation.

Evaporation. The boundary conditions of the Crout model, which characterise the kinetics of the phase transition [7, 8], in the case of evaporation have the form

$$\frac{T}{T_c} = \frac{2\gamma M^2 (m^2 + 1/2)^2}{(1 + \gamma M^2)^2 m^2 t^2},$$

$$\frac{\rho}{\rho_{sat}} = \frac{tm^2(1 + \gamma M^2)[\gamma M^2 (m^2 + 1/2)]^{-1}}{\exp(-m^2) + \pi^{1/2} m(1 + \operatorname{erf} m)},$$

$$M = v/(\gamma RT)^{1/2}, \quad \rho_{sat} = p_{sat}/(RT_c), \tag{17}$$

$$p_{sat} = p_b \exp\left[\frac{L_v}{RT_c}\left(1 - \frac{T_b}{T_c}\right)\right],$$

where ρ_{sat} and p_{sat} are the saturated vapour density and pressure at the temperature T_c; R is the gas constant; γ is the adiabatic exponent (equal to 5/3 for monatomic vapour); p_b and T_b are the equilibrium pressure and temperature of evaporation under normal conditions; the Mach number is determined by solving gas-dynamic equations, while the parameter m from the equation

$$f(m) = F(M)(m^2 + 1/2)^2 - m^2(m^2 + \alpha + 3/2) = 0,$$

$$F(M) = 1 + \frac{3\gamma M^2 - 1}{\gamma M^2 + 1}, \quad \alpha = 2t^2 - 2^{-1}\pi^{1/2} mt - 1, \tag{18}$$

$$t = \frac{2m}{\pi^{1/2}} + \frac{1 + \operatorname{erf} m}{\exp(-m^2) + \pi^{1/2} m(1 + \operatorname{erf} m)}.$$

Condensation. On reaching the inequality $p_{sat} < p$ there occurs a change in the direction of the phase transition: evaporation is replaced by vapour condensation on the surface ($M < 0$). Unlike evaporation, the surface condensation may take place in the supersonic regime as well. According to Ref. [10], the quantities T, M, and p in the regime of subsonic condensation are related only by one equation: $p/p_{sat} = F(T/T_c, M)$, in which the variables T/T_c and M are determined by the state of gas dynamic flow. The function $F(T/T_c, M)$ is determined in advance from the solution of the Boltzmann equation and is tabulated. Its values depend only slightly on the temperature, depend much stronger on the parameter M, and qualitatively change upon transition through the $M = -1$ value. In the supersonic regime the boundary conditions change, because all the quantities at the boundary in this case depend on the state of the gaseous medium away from the surface and are found by extrapolation. Therefore, the boundary conditions for the surface condensation in the subsonic regime are determined with the help of the tabulated function

$$p/p_{sat} = F(T/T_c, M), \tag{19}$$

and in the supersonic regime the quantities T, M, and p are extrapolated with the help of gas-dynamic equations. The extrapolation method of determining the boundary conditions is also used in subsonic regimes when the inequality $p/p_{sat} > 10$ is fulfilled.

2.4 Algorithm of numerical solution

The system of differential equations (1)–(19) was solved by the finite difference method. The computational grid contained 50–100 nodes along the r axis in the region $0 < r < L_r = 5$ cm and was more dense in the region of the laser spot. The nonuniform grid along the z axis was separately constructed in the condensed ($l_z = 0.01$ cm, 40 nodes) and gaseous ($L_z = 10$ cm, 100–200 nodes) media. In both regions, the grid became dense torward the target surface; the first step being equal to 2×10^{-6} and 10^{-5} cm, respectively. The heat conduction equation with a convective term and variable coefficients was approximated by a totally implicit difference scheme written on a five-point pattern [37]. It was solved by the alternating direction method with iterations. The approximation and algorithm for solving the difference equations of radiative gas dynamics are given in [32, 38]. The solution algorithm of the problem as a whole took into account the interrelation of the processes and included three stages at each time step: the solution of equations in the gaseous medium, the calculation of relationships at the interphase boundary, and

the solution of the equation in the condensed medium. All the three stages were further repeated in the outer loop [16].

3. Analysis of results and their discussion

In our numerical experiments we investigated the pulsed action of KrF-laser radiation with a Gaussian intensity distribution in time and space. The pulse duration was 20 ns, the peak intensity was $G_0 = 2 \times 10^8 - 10^9$ W cm^{-2}, and the beam radius was $r_f = 0.005$, 0.025, and 0.25 cm. In this case, the version with $G_0 = 5 \times 10^8$ W cm^{-2} and $r_f = 0.025$ cm was considered as the reference one. The parameters of aluminium used in calculations were $T_b = 2720$ K, $p_b = 1$ bar, and $L_v = 1.1 \times 10^4$ J g^{-1} [39]. The values of the thermal conductivity, heat capacity and density were specified taking into account the difference between the solid ($T_c < T_m$) and liquid ($T_c > T_m$) phases: $\Lambda_c = 2.37$ and 0.75 W cm^{-1} K^{-1}, $c_p = 0.95$ and 1.2 J g^{-1} K^{-1}, $\rho = 2.7$ and 2.33 g cm^{-3} (the melting temperature $T_m = 933$ K) [39]. The temperature dependence of surface absorptivity $A(T_c)$ was described by the expressions: $A(T_c < T_m) = 0.231$ and $A(T_c > T_m) = 0.64 T_c^{0.4}$ [25]. According to the second relation, for $T_c = 6000$ K the surface absorbs approximately half the incident radiation ($A \approx 50\%$).

3.1 Main stages of evaporation and condensation on the surface

We will describe the main stages of the processes at the target surface ($z = 0$) by the time dependences of the Mach number $M(t, r = 0)$, the temperature of condensed medium at the surface $T_c(t, r = 0)$, and the ratio between the saturated vapour pressure to the plasma pressure $p_{sat}(t, r = 0)/p_{pl}(t, r = 0)$ at the target centre ($z = 0$, $r = 0$) (Fig. 3). The material evaporation begins shortly after the onset of irradiation, and almost immediately the Mach number attains a value of unity (Fig. 3a), but the evaporation stage with a sound velocity turns out to be very short. Due to its high photon energy, the UV radiation with $\lambda = 0.248$ μm initiates photoprocesses in the evaporated material and comes to experience absorption even in relatively cool vapour. The release of laser pulse energy is accompanied by the further vapour heating and a stronger absorption, which eventually results in the production of plasma characterised by high (compared to the pre-plasma state) temperature and pressure. The response to the emergence of counterpressure of the plasma medium is a sharp decrease in the Mach number at the evaporating surface, which becomes equal to $\sim 0.1 - 0.15$ after a short transition period. The evaporation continues with this Mach number in an essentially subsonic regime approximately till the end of the pulse. After irradiation, the Mach number passes into the region of negative values corresponding to condensation.

Let us compare the behaviour of the parameter M with the temperature and pressure dynamics at the surface and in the plasma. The plasma production is almost unnoticeable in the temperature curve T_c (Fig. 3a), which continues to monotonically increase for ~ 20 ns and only then, following the lowering of incident radiation intensity, begins to decrease. On the other hand, two evaporation stages are clearly seen in the pressure ratio curve (Fig. 3b). During the evaporation period ($M = 1$), the saturated vapour pressure is several times higher than the plasma counterpressure,

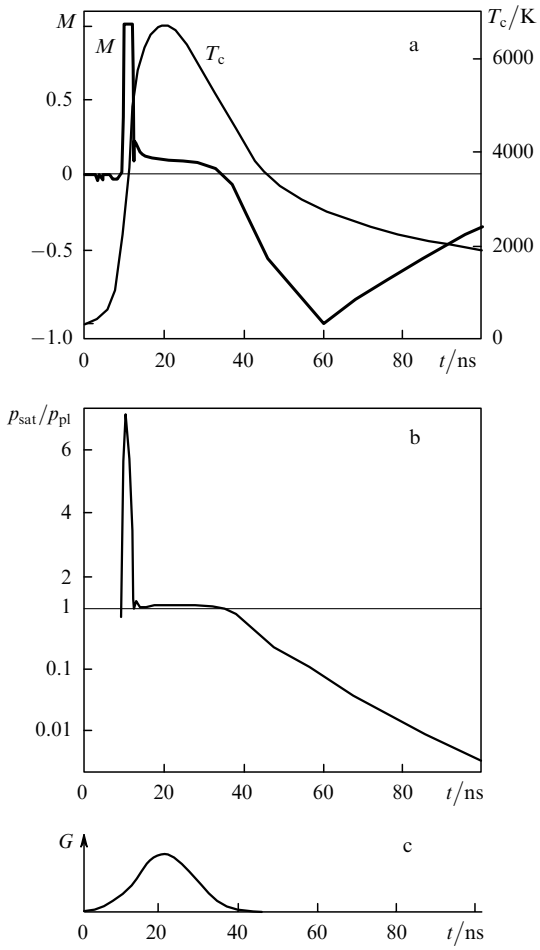

Figure 3. Time dependences of the Mach number $M(t, r = 0)$, the surface temperature $T_c(t, r = 0)$ (a), and the pressure ratio $p_{sat}(t, r = 0)/p_{pl}(t, r = 0)$ (b) at the target centre for $G_0 = 5 \times 10^8$ W cm^{-2} and $r_f = 0.025$ cm, as well as the laser pulse profile $G(t)$ (c).

while at the stage of subsonic evaporation these pressures are comparable: $p_{sat}/p_{pl} \geqslant 1$. The condensation stage is characterised by the pressure ratio smaller than unity. The saturated vapour pressure, which lowers exponentially with surface cooling, decreases faster than the plasma pressure, and therefore the ratio p_{sat}/p_{pl} also decreases with time to become equal to 0.1 at the instant $t \approx 55$ ns. In this case, the Mach number at the outer side of the KL reaches a value of -1. The condensation on the target surface passes into the supersonic regime, which is realised by transforming the boundary condition described by expression (19) to the extrapolation procedure.

The analysis of the spatiotemporal dependences $v(t, r = 0, z)$, $p(t, r = 0, z)$, $T(t, r = 0, z)$, $M(t, r = 0, z)$ at the instants $t = 40$, 60, and 100 ns (Fig. 4) shows that the supersonic flow develops and persists in a relatively narrow spatiotemporal range. Due to gas-dynamic expansion and radiative losses, all spatial near-surface plasma characteristics equalise and decrease within 40 – 100 ns: the velocity decreases by an order of magnitude, the pressure by about 2.5 orders of magnitude, the temperature approximately 1.5-fold, and the Mach number in the negative value range from -1.1 to -0.35. Therefore, the short period of supersonic surface condensation is replaced by a subsonic condensation regime because of spatial effects away from the surface. Note that the lowering of condensation rate is

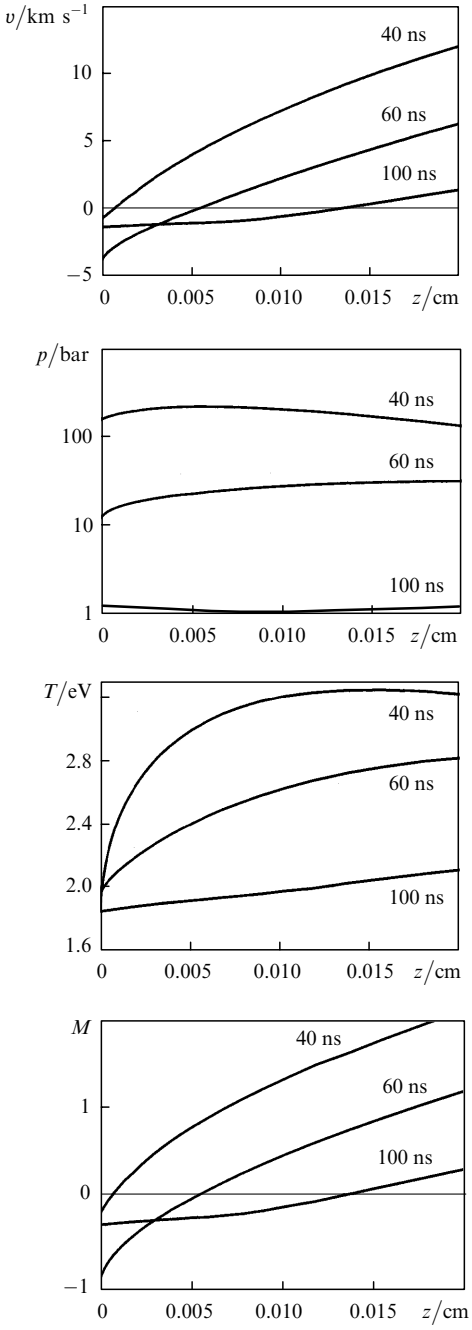

Figure 4. Distributions of the z-component of the velocity $v(t, r = 0, z)$, the pressure $p(t, r = 0, z)$, the temperature $T(t, r = 0, z)$, and the Mach number $M(t, r = 0, z)$ in the plasma on the axis of the laser beam at different instants.

not related to the pressure drop across the KL, where the ratio p_{sat}/p_{pl} continues to decrease due to the fast surface cooling and achieves the value 0.01 (Fig. 3b).

Figure 5 shows the time dependences of the Mach number at the centre of the target for different irradiation intensities G_0 and beam radii r_f. For all the intensities exceeding the plasma production threshold, the main stages of the processes at the surface correspond to the base calculation. In this case, the evaporation begins earlier with increasing intensity, the duration of the evaporation stage with $M = 1$ shortens, and the condensation stage after irradiation becomes longer (Fig. 5a). Decreasing the focal

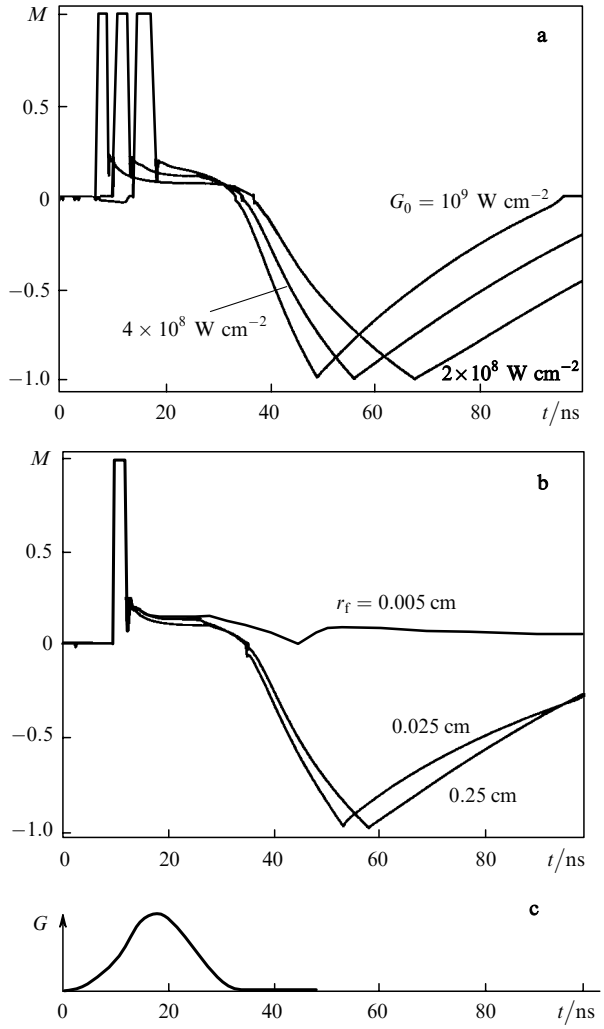

Figure 5. Time dependences of the Mach number at the centre of the target $M(t,\ r = 0)$ for different irradiation intensities G_0 and $r_f = 0.025$ cm (a) and for different beam radii r_f and $G_0 = 5 \times 10^8$ W cm^{-2} (b) as well as the laser pulse profile $G(t)$ (c).

spot radius r_f enhances the effect of radial expansion of the evaporated material and reduces condensation (Fig. 5b).

One of the most important optical characteristics of a plasma is its transmission coefficient, which shows what part of the laser energy reaches the target surface and is spent to heat and remove the material. The transmission coefficients $T_{pl}(t, r) = G^-(t, r, z = 0)/G^-(t, r, z = L_z)$ of a plasma determined at the beam centre ($r = 0$) and at distances $r = r_f/2$ and $r = r_f$ from the beam centre are plotted in Fig. 6 ($G_0 = 5 \times 10^8$ W cm^{-2}, $r_f = 0.025$ cm). At the beam centre, the screening plasma action is revealed even at the initial stage of irradiation: the transmission coefficient begins to decrease from instant $t \approx 10$ ns, achieves a minimum (about 30 %) at the pulse maximum, and then increases gradually. The behaviour of transmission coefficients at the two other radial points is qualitatively similar to their behaviour at the centre, but the screening action at these points is revealed later and to a smaller degree: about 70 % of the incident radiation and more reaches the surface at the distance $r = r_f$.

3.2 Two-dimensional effects: surface evaporation

The development of evaporation within the entire irradiated region is illustrated by the dependences of the Mach

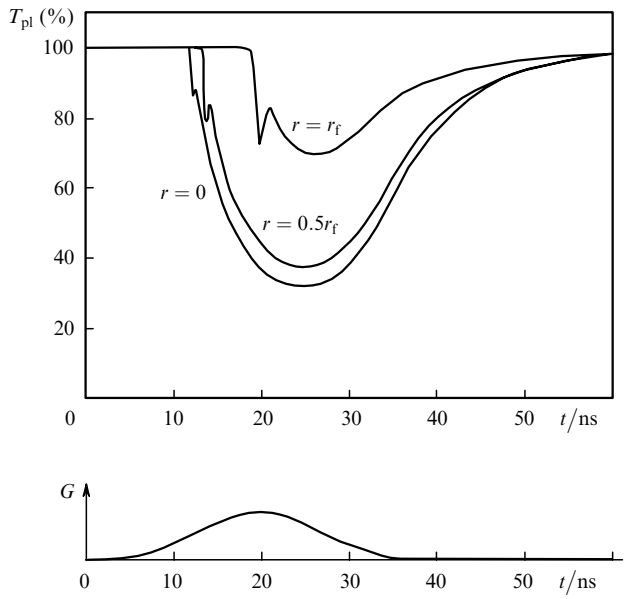

Figure 6. Time dependences of the plasma transmittance $T_{pl}(t,r) = G^-(t,r,z=0)/G^-(t,r,z=L_z)$ for different r, $G_0 = 5 \times 10^8$ W cm^{-2}, $r_f = 0.025$ cm and the profile of the laser pulse $G(t)$.

number $M(t,r)$ and the pressure ratio $p_{sat}(t,r) \times p_{pl}^{-1}(t,r)$ at instants in time $t = 12$, 20, and 30 ns (Fig. 7). At $t = 12$ ns, the evaporation, which proceeds at a sound velocity, already embraces the greater part of the laser spot, and the Mach number at the centre began to decrease due to the growing plasma pressure. At the instant $t = 20$ ns, which corresponds to the laser pulse maximum, the evaporation at a sound velocity persists only in a narrow circular band at the periphery of the laser spot [Fig. 7a, curve (*2*)], where the saturated vapour pressure is 5–6 times higher than the plasma pressure [Fig. 7b, curve (*2*)]. In the remaining part of the spot, the saturated vapour pressure and the plasma pressure are comparable: $p_{sat}/p_{pl} \approx 1$ (but higher than 1), and the evaporation intensity is about the same ($M \approx 0.1 - 0.15$). A similar picture also persists for $t =$ 30 ns [Figs 7a and 7b, curves (*3*)].

The dependences of the surface temperature $T_c(t,r)$ and absorbed intensity $AG^-(t,r,z=0)$ calculated for $t = 10$, 20, and 30 ns (Fig. 8) demonstrate the plasma influence on the action of laser radiation on the target. Prior to plasma production, the temperature distribution accurately replicates the laser pulse profile [Fig. 8a, curve (*1*)], while the temperature distribution over the spot at later instants [curves (*2*) and (*3*)] becomes substantially more uniform and has the form of a flattened bell. Such a distribution results from the nonuniformity of plasma transmission (see Fig. 6): the higher-intensity radiation at the beam centre is

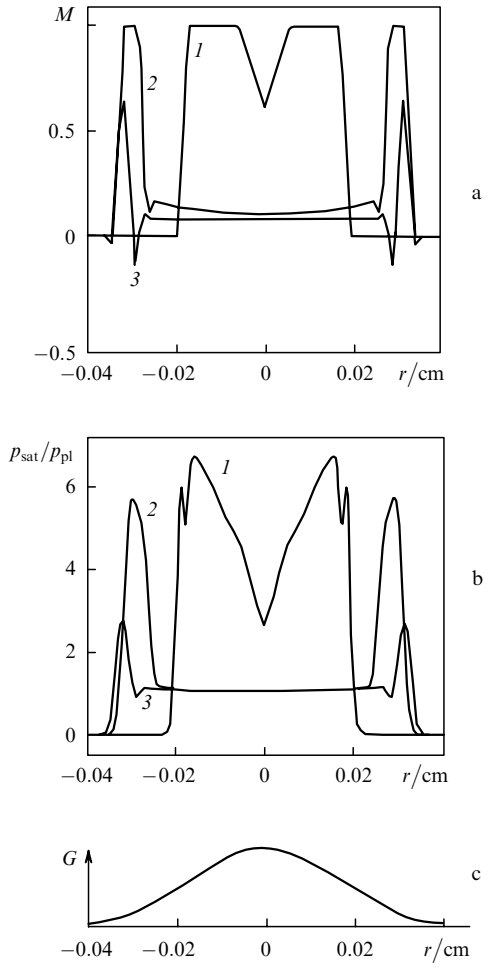

Figure 7. Spatial distributions of the Mach number $M(t, r)$ (a) and the pressure ratio $p_{sat}(t,r)/p_{pl}(t,r)$ (b) at different instants $t = 12$ (*1*), 20 (*2*), and 30 ns (*3*) for $G_0 = 5 \times 10^8$ W cm^{-2} and $r_f = 0.025$ cm as well as the laser pulse profile $G(r)$ (c).

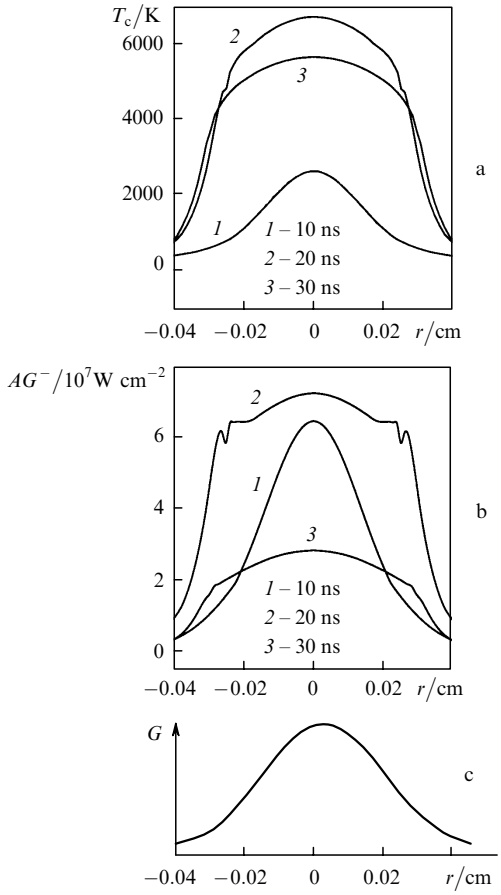

Figure 8. Spatial distributions of the temperature $T_c(t,r)$ (a) and the intensity of laser radiation absorbed at the surface $AG^-(t,r)$ (b) at different instants for $G_0 = 5 \times 10^8$ W cm^{-2} and $r_f = 0.025$ cm as well as the laser pulse profile $G(r)$ (c).

screened stronger than at the beam periphery, which partially equalises the absorbed radiation profile [Fig. 8b, curves (*2*) and (*3*)].

The vapour condensation on the surface after the end of the pulse is illustrated by the dependence $M(t, r)$ calculated at different distances from the centre (Fig. 9). The curve for $r = r_f$ is similar to the dependence $M(t, r = 0)$ for the target centre in Fig. 3. At longer distances from the centre (Fig. 9, the curves for $r = r_f$ and $2r_f$), no target evaporation occurs (the positive part of the curves is missing), and the condensation begins with a significant time delay (at the moment when the expanding plasma cloud travels the corresponding distance). The variation of pressure above the surface $p_{pl}(t, r, z = 0)$ and its temperature $T_c(t, r, z = 0)$ are plotted in Fig. 10 for $t = 40$, 60, and 100 ns. A comparison of curves (*2*) and (*3*) (Fig. 10a) shows that the plasma region is approximately two times larger than the evaporation region because of the radial expansion and the substance from the plasma beyond the evaporation region condenses on a nearly cool surface (Fig. 10b).

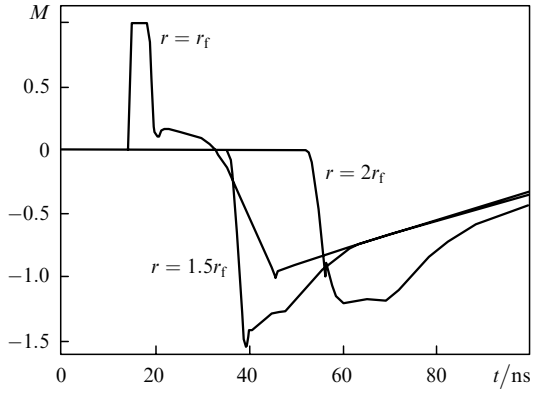

Figure 9. Time dependences of the Mach number $M(t, r)$ at different points on the surface for $G_0 = 5 \times 10^8$ W cm^{-2} and $r_f = 0.025$ cm.

The time-integrated phase transformation effect is demonstrated by the time dependences of ablated layer thickness H_v obtained by integrating the front velocity: $H_v = \int V_c dt$ (Figs 11a and 11b). The distributions $H_v(t, r)$ for $G_0 = 5 \times 10^8$ W cm^{-2} and $r_f = 0.025$ cm at different instants $t = 14$, 20, 40, and 100 ns show that the layer thickness increases during the pulse action to achieve a value of 1.3×10^{-5} cm at the instant of its completion $t = 40$ ns and the width of the produced cavity is equal to $\sim 3 \times 10^{-2}$ cm. At the instant $t = 100$ ns, the layer thickness at the cavity centre decreases slightly due to condensation and small projections appear along its edge. The time dependences of the layer thickness at the centre $H_v(t, r = 0)$ are plotted in Fig. 11b for different irradiation parameters. Increasing the focal spot radius r_f above 0.025 cm does not result in an appreciable growth in the evaporated layer thickness [Fig. 11b, curves (*2*) and (*3*)]. The high plasma pressure moderates evaporation in these cases and simultaneously enhances the role of surface condensation, which manifests itself in the lowering of the H_v values with time. Decreasing the parameter r_f by a factor of two leads to a significant weakening of plasma effects due to the enhancement of radial expansion and the consequential decrease in the effect of surface condensation

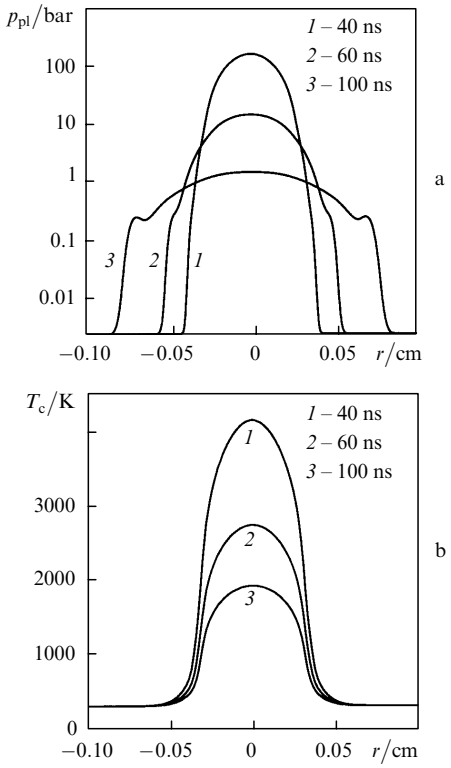

Figure 10. Spatial distributions of the plasma pressure at the boundary of the KL $p_{pl}(t, r, z = 0)$ (a) and suface temperature $T_c(t, r, z = 0)$ (b) at different instants after pulse completion for $G_0 = 5 \times 10^8$ W cm^{-2} and $r_f = 0.025$ cm.

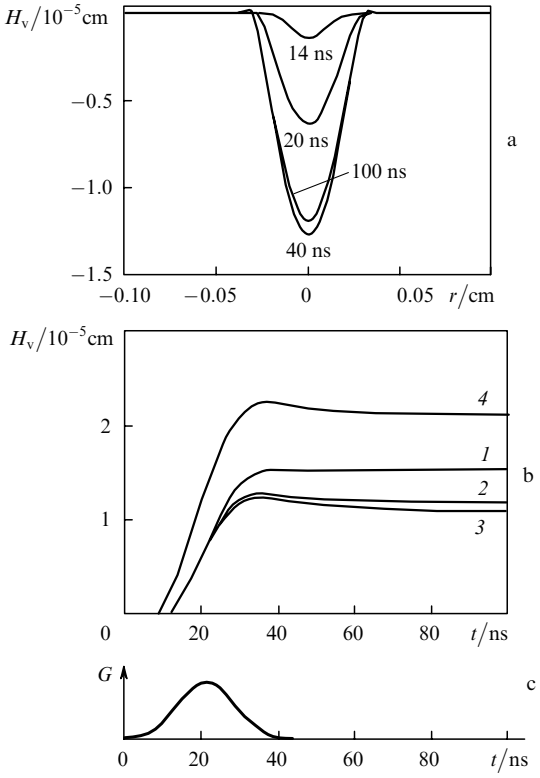

Figure 11. Spatial distributions of the evaporated layer thickness $H_v(t, r)$ at different instants for $G_0 = 5 \times 10^8$ W cm^{-2} and $r_f = 0.025$ cm (a) and the time dependences $H_v(t, r = 0)$ for irradiation intensities $G_0 = 5 \times 10^8$ (*1–3*) and 10^9 W cm^{-2} (*4*) and the beam radii $r_f = 0.005$ (*1*), 0.025 (*2*, *4*), and 0.25 cm (*3*) (b) as well as the laser pulse profile $G(t)$ (c).

and the increase in the evaporated layer thickness by about 25 % [curve (*1*)]. As the irradiation intensity G_0 is increased to 10^9 W cm^{-2}, the ablated layer also increases approximately twice [curve (*4*)].

3.3 Two-dimensional effects: plasma

Consider the spatiotemporal evolution of the plasma cloud, which has a decisive effect on the phase transformations of the surface. The plasma state can be characterised by analysing two-dimensional distributions of the temperature $T(t,r,z)$, the pressure $p(t,r,z)$, and the vapour velocity $V(t,r,z)$ plotted in Fig. 12 and related to the two instants: $t = 25$ and 60 ns. The temperature distribution shows that the hottest plasma region during exposure is located in the immediate vicinity of the surface and has a relatively low temperature – about 3 eV. It was found that the laser radiation energy was released in this region. The heated region with a high density determined by the vapour emanating from the surface is responsible for the formation of a high-pressure (above 1000 bar) region near the surface, which substantially slows down the evaporation and determines so small a Mach number at the subsonic evaporation stage. The cloud expands primarily away from the surface, the expansion velocity in the lateral dimension being insignificant. After irradiation ($t = 60$ ns) the picture in the plasma becomes substantially different (Figs 12c and d). The highest temperature and density region is displaced from the surface and expands not only towards the outer boundaries, but towards the target surface as well.

A more exact quantitative picture of processes in the plasma is provided by the distributions of the temperature $T(t, r = 0, z)$, the density $\rho(t, r = 0, z)$, and the z-component of velocity $v(t, r = 0, z)$ at different instants $t = 20$, 30, 60, and 100 ns along the laser beam axis ($r = 0$) (Fig. 13). They show, in particular, that the temperature maximum for $t = 20$ and 30 ns is equal to 3.2 – 3.5 eV and is located at a distance of ~ 0.01 cm from the surface for the characteristic density $\rho = 1 - 5 \times 10^{-3}$ g cm^{-3}. The plasma cloud expands both during the pulse and after its completion. For $t = 100$ ns its dimension amounts to 0.25 cm $= 10 r_f$. The

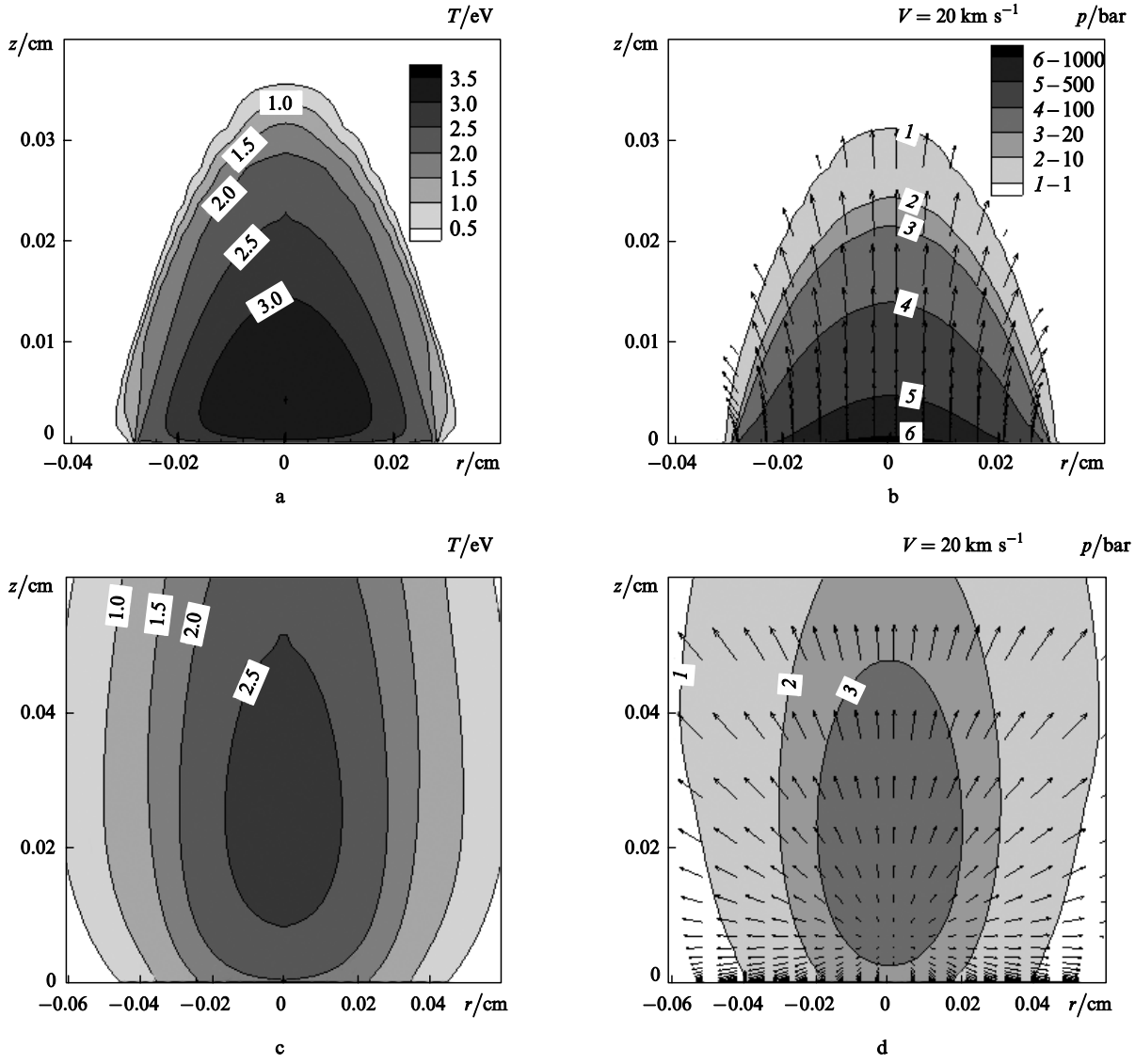

Figure 12. Distributions of the temperature $T(t, r, z)$ (a, c), the pressure $p(t, r, z)$ and the velocity vector $V(t, r, z)$ (b, d) in a plasma at the instants $t = 25$ (a, b) and 60 ns (c, d) for $G_0 = 5 \times 10^8$ W cm^{-2} and $r_f = 0.025$ cm.

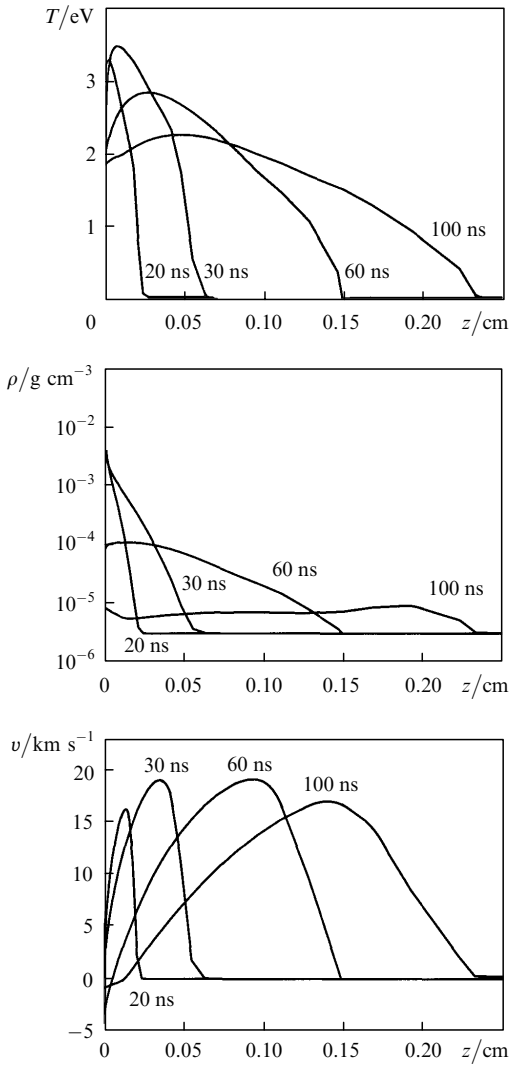

Figure 13. Distributions of the temperature $T(t, r = 0, z)$, the density $\rho(t, r = 0, z)$, and the z-component of the velocity $v(t, r = 0, z)$ of plasma at different instants for $G_0 = 5 \times 10^8$ W cm^{-2} and $r_f = 0.025$ cm.

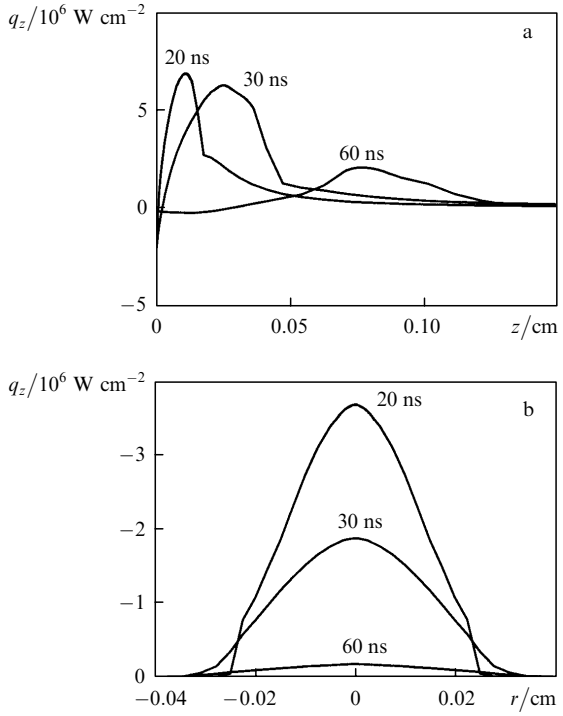

Figure 14. Distributions of the z-component of the radiative flux of the plasma on the laser beam axis $q_z(t, r = 0, z)$ (a) and at the target surface $q_z(t, r, z = 0)$ (b) at different instants for $G_0 = 5 \times 10^8$ W cm^{-2} and $r_f = 0.025$ cm.

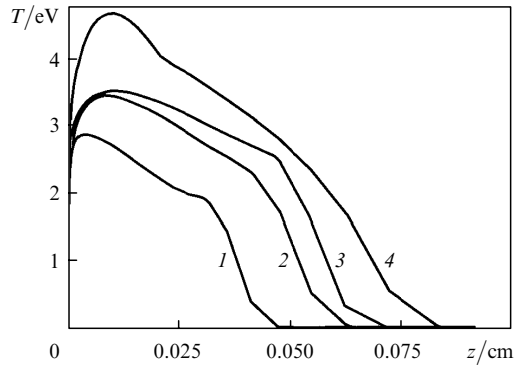

Figure 15. Distributions of the plasma temperature $T(t = 30$ ns, $r = 0$, $z)$ on the laser beam axis for irradiation intensities $G_0 = 5 \times 10^8$ (*1–3*) and 10^9 W cm^{-2} (*4*) and the beam radii $r_f = 0.005$ (*1*), 0.025 (*2*, *4*), and 0.25 cm (*3*).

expansion is accompanied by a slow plasma cooling to about 2 eV. The expansion velocity decreases still slower, achieving 15 km s^{-1}, which results in a rapid lowering of the plasma density to $\sim 10^{-5}$ g cm^{-3} for $t = 100$ ns.

The dependences of the z-component of radiative flux on the laser beam axis $q_z(t, r = 0, z)$ (Fig. 14a) and at the target surface $q_z(t, r, z = 0)$ (Fig. 14b) permit analysing the magnitude and role of thermal radiation in the plasma. During irradiation, the radiative flux $q_z^{\max} \approx 6.8 \times 10^6$ W cm^{-2} forms in the near-target region and is emitted towards the outer boundaries (Fig. 14a). The kink in the curves corresponds to the location of the cloud boundaries at a given instant. The maximum flux directed to the target is approximately two times weaker (3.5×10^6 W cm^{-2}) and irradiates the same surface area as the laser radiation. The radiative flux is significantly weaker in magnitude than the laser flux due to the relatively low plasma temperature.

We consider the variations of plasma cloud parameters upon variations of the intensity and radius of the laser beam by the example of temperature distributions T ($t = 30$ ns, $r = 0$, z) (Fig. 15). As the irradiation intensity was doubled (to 10^9 W cm^{-2}), the maximum temperature increased by a factor of 1.5 (approximately to 4.5 eV). During the two-dimensional expansion at a small irradiation radius ($r_f = 0.005$ cm), the plasma temperature is lower and the dimension of the plasma region decreases, whereas for $r_f = 0.025$ and 0.25 cm the distributions are almost similar. For all irradiation regimes, the temperature maximum (and the energy release region) is located near the surface.

4. Comparison of the two-dimensional model with theory and experiment

Irradiation of aluminium targets in vacuum by nanosecond pulses from excimer lasers was studied in several experimental works [40–43]. However, none of these papers

contains the entire set of quantitative characteristics of the laser-produced plasma plume, and therefore we performed a comparison with them only regarding separate aspects.

4.1 Emissivity of a plasma

The emissivity of a plasma can be characterised by the radiation value ε, which is the ratio of the plasma radiation flux $q_z^{\max}$ to the equilibrium black-body radiation flux $q_b = \sigma T^4$, where σ is the Stefan–Boltzmann constant. For $t = 20$ ns, $T_{\max} = 3.3$ eV, $q_b = 1.25 \times 10^7$ W cm^{-2}, we obtain $q_z^{\max} = 6.75 \times 10^6$ W cm^{-2}, $\varepsilon = q_z^{\max}/q_b = 0.54$, and for $t = 30$ ns, $T_{\max} = 3.5$ eV, $q_b = 1.58 \times 10^7$ W cm^{-2} we have $q_z^{\max} = 6.0 \times 10^7$ W cm^{-2}, $\varepsilon = q_z^{\max}/q_b = 0.38$. Therefore, the highest radiation flux which escapes from the plasma is equal to about half the theoretically possible flux.

The calculated values of the emissivity of the plasma can be compared with the data of a theoretical paper [44] (see Fig. 10b therein), in which a simplified two-layer model was employed to investigate the temperature dependence of the emissivity of plasmas of different optical thickness in the temperature range 2–20 eV corresponding to laser irradiation of aluminium vapour in vacuum with an intensity of $10^6 - 10^{10}$ W cm^{-2}. In particular, for a temperature $T = 3.5$ eV, a density $\rho = 1.2 \times 10^{-3}$ g cm^{-3}, and a plasma layer thickness $L_{pl} = 0.03$ cm, the radiation value $\varepsilon \approx 0.65$ and for smaller thickness ($L_{pl} = 0.01$ cm) there results $\varepsilon \approx 0.4$. These values are in rather good agreement with our calculations.

4.2 Threshold of plasma production

Ref. [40] was concerned with the irradiation of an aluminium target by 15-ns long KrF-laser pulses with $\lambda = 0.248$ μm. For this regime, the threshold of plasma formation was determined, which was identified by a sharp rise in emission intensity and evaluated at 1.2×10^8 W cm^{-2}. About the same threshold intensity value ($G \approx 10^8$ W cm^{-2}) determined from a sharp temperature rise in the vaporised material was obtained from calculations. With the help of spectroscopic techniques in Ref. [41] it was determined that at a higher intensity there occurs production of a strongly ionised dense plasma in the state of thermodynamic equilibrium. The characteristic plasma temperature calculated for this regime was equal to ~ 2.5 eV.

4.3 Spatiotemporal plasma characteristics

The authors of paper [42] report the experimental data on aluminium target irradiation by 0.308-μm, 20-ns pulses from a XeCl laser with the intensity of $10^8 - 10^9$ W cm^{-2}. Spectral and probe measurements of the electron temperature and density were performed at a distance of 0.02 cm from the target beginning from the instant $t \approx 50$ ns, when the emission intensity was at its maximum. The electron temperature T_e^{exp} was determined from the relative intensity of the $\lambda = 466$-nm and 559-nm spectral lines of singly ionised aluminium atoms. The electron concentration N_e^{exp} at different instants was estimated from the absorption of the 594-nm dye-laser radiation in the plume taking into account the plasma temperature and the plasma expansion dynamics.

By simulating the irradiation regime with $G_0 = 9 \times 10^8$ W cm^{-2} within the framework of a locally equilibrium model (1)–(19) supplemented with the system of Saha equations, we determined the spatiotemporal distribution of equilibrium values of temperature T and electron density N_e. A comparison of the calculated dependences $T(t, r = 0, z = 0.02$ cm) and N_e $(t, r = 0, z = 0.02$ cm) with the experimental ones (Fig. 16a) showed that the calculated temperature exceeds the experimental one by 20%–25% during the 50–120-ns period, but later on the temperature difference somewhat increases. The calculated electron concentration exceeds the experimental one by a factor of two–three. According to the calculated data, the maximum values of the plasma characteristics under investigation are achieved during the time $t \approx 25 - 30$ ns of the pulse action and exceed (twice in temperature, by an order of magnitude in concentration) the experimental values at the initial instant of observation $t \approx 50$ ns.

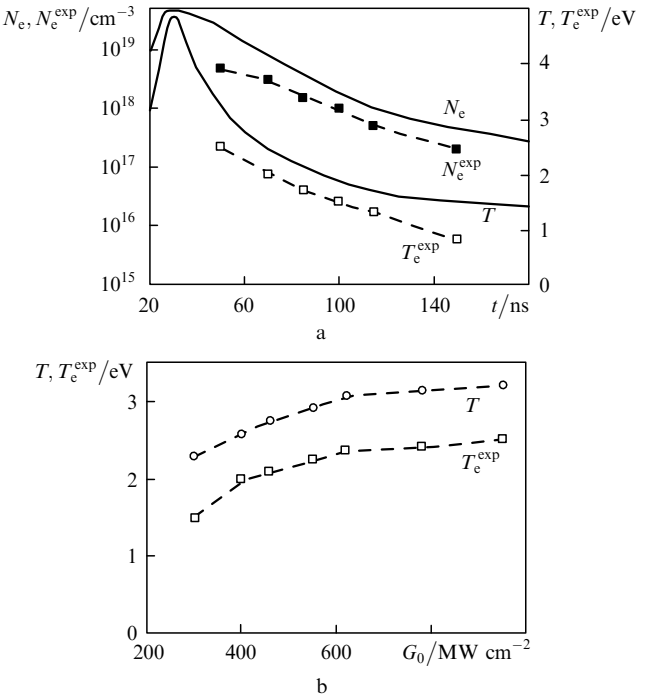

Figure 16. Comparison of experimental [42] time dependences of the electron temperature T_e^{exp} and density N_e^{exp} with the calculated curves $T(t, r = 0, z = 0.02\,\text{cm})$ and $N_e(t, r = 0, z = 0.02\,\text{cm})$ for $G_0 = 9 \times 10^8$ W cm^{-2}, $\lambda = 0.308$ μm, and a pulse duration $\tau = 20$ ns (a) as well as experimental [T_e^{exp} ($t = 50$ ns)] and calculated [$T(t = 50$ ns, $r = 0$, $z = 0.02$ cm)] plasma temperatures vs intensity G_0 (b).

The calculated temperature values T ($t = 50$ ns, $r = 0$, $z = 0.02$ cm), obtained for different laser radiation intensities G_0 exceed the corresponding values by 0.7–0.8 eV (Fig. 16b). In this case, the run of the two curves is similar and shows that the efficiency of laser-induced plasma heating gradually decreases as the temperature increases.

4.4 Energy input into the target and the plasma

The main channels of energy distribution and transformation in the system laser radiation–erosion plasma–

Table 1.

Data	A_h	A_v	A_{pl}	R_{ref}	H_v/μm
Experimental	0.2 ± 0.05	0.21 ± 0.1	0.29 ± 0.1	0.3 ± 0.05	0.8 ± 0.25
Calculated	0.08	0.12	0.51	0.29	0.3

target upon irradiation by 20-ns XeCl-laser pulses with an intensity of 10^9 W cm^{-2} were studied in papers [30, 43].

The experimental and calculated values of different energy components of laser radiation are given in Table 1. Taking for simplicity the total laser pulse energy E to be equal to unity, we can write the expression for the energy balance in the system in the form:

$$E = 1 \approx A_h + A_v + R_{ref} + A_{pl}, \quad (20)$$

where A_h is the thermal energy transferred to the target, which is experimentally measured with a thermocouple; A_v is the energy spent on the heating and evaporation of the layer whose thickness H_v was determined by measuring the crater depth; R_{ref} is the reflected energy determined with the help of an integrating sphere surrounding the target; and A_{pl} is the energy which is released in the plasma as the incident and reflected beams pass through the plasma and is determined from expression (20).

The same quantities were determined by way of calculations: A_h and A_{pl} by spatial integration of the internal target energy and the total plasma energy at the instant of simulation termination, A_v by surface and time integration of the energy expenditures related to the flow of evaporated material, and R_{ref} from expression (20).

A comparison of calculated and experimental data demonstrates that the calculations overestimate the energy fraction absorbed by the plasma and underestimate the energy fraction that goes to heat and vaporise the target. The underestimation of the energy input into the target is also confirmed by the fact that the calculated thickness of the vaporised layer turns out to be approximately two times smaller. The most likely reasons for the discrepancy between the theoretical and experimental data are a rather rough temperature dependence of surface absorptivity $A(T_c)$ and the use of a locally thermodynamic-equilibrium model of radiative gas dynamics to describe the plasma behaviour.

An illustration of how strongly the plasma may affect the evaporation is provided by the comparison of the dependences of the evaporated layer thickness at the spot centre $H_v(t, r = 0)$ (Fig. 17) calculated by the model (1)–(19) with the inclusion of plasma production and by neglecting laser radiation absorption in the vapour and plasma production. In the absence of plasma, the evaporated layer thickness increases approximately four-fold and exceeds 1 μm.

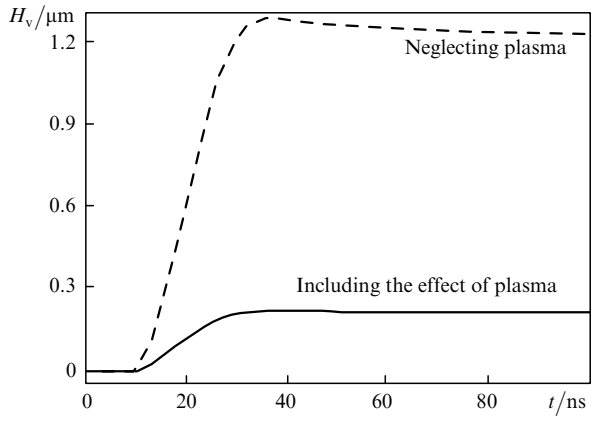

Figure 17. Time dependences of the evaporated layer thickness $H_v(t, r = 0)$ calculated with the inclusion (solid curve) and with neglect (dashed line) of laser radiation absorption in the plasma for $G_0 = 5 \times 10^8$ W cm^{-2}, $r_f = 0.025$ cm.

By and large we can argue on the basis of the comparison performed above that the results of simulation are in qualitative, and in several aspects in quantitative, agreement with available experimental data.

5. Conclusions

We have revealed the following properties of the phase transitions on the aluminium surface and the processes in the plasma irradiated by 20-ns KrF-laser pulses with an intensity of $2 \times 10^8 - 10^9$ W cm^{-2}:

– The laser plasma produced in aluminium vapour under UV laser irradiation is not optically thick enough to completely screen the surface. As a consequence, the target evaporation proceeds during the laser pulse and exhibits two characteristic stages: evaporation with the sound velocity ($M = 1$) at the beginning and subsonic evaporation ($M \ll 1$) after the plasma production.

– Once the plasma is produced, the subsonic evaporation regime with a velocity only slightly varying with $|r|$, whereby $M \approx 0.1 - 0.15$, is established on almost the entire surface under irradiation ($|r| < r_f$), with the exception of a narrow peripheral zone near the beam boundary ($|r| > r_f$). In the peripheral zone, the influence of absorbed radiation with a relatively low intensity is balanced out by a rapidly decreasing pressure, resulting in the formation of highest-velocity evaporation ($M \approx 1$).

– The plasma structure during irradiation is characterised by the presence of a thin region adjacent to the surface in which the main fraction of laser energy is released and the highest, relatively low temperature is achieved ($\sim 3 - 4.5$ eV). The corresponding pressure of ~ 1 kbar proves to be sufficient to substantially moderate the emanation of vapour from the surface. The effect of counterpressure depends on the focal spot radius. In the irradiation regimes under consideration it becomes negligible for $r_f < 0.01$ cm.

– The overall effect of laser plasma on evaporation manifests itself in a significant (by a factor of 2–4) reduction of material removal from the irradiation region.

– The surface condensation in the case of UV laser irradiation begins after the end of the pulse. The evaporated material condenses on the surface, both in the evaporated cavity and some distance away due to the lateral expansion of the plasma cloud.

– The intrinsic plasma radiation flux, which is formed in the plasma core and is radiated towards the outer boundaries, amounts to 50 % and more of the equilibrium Planck radiation flux, the flux towards the target is approximately two times lower. Because of the moderate temperature, the effect of plasma radiation on the processes occurring under irradiation by nanosecond laser pulses is substantially weaker than upon irradiation by microsecond pulses.

Acknowledgements. This work was supported by the Russian Foundation for Basic Research (Grant No. 04-01-00701).

References

1. Afanas'ev Yu.V., Krokhin O.N., in *The Physics of High Energy Densities*. Ed. by P. Caldirola and H. Knoepfel (New York: Academic Press, 1971; Moscow: Mir, 1974).
2. Romanov G.S., Pustovalov V.K. *Izv. Akad. Nauk BSSR, Ser. Fiz.-Mat. Nauk*, (4), 84 (1967).
3. Anisimov S.I. *Zh. Eksp. Teor. Fiz.*, **54**, 339 (1968).
4. Knight Ch.J. *AIAA J.*, **17**, 519 (1979).
5. Samokhin A.A. *Kratk. Soobshch. Fiz.*, (6), 3 (1982).
6. Moizhes B.Ya., Nemchinskii V.A. *Zh. Tekh. Fiz.*, **52**, 684 (1982).
7. Crout D. *J. Math. Phys.*, **15**, 1 (1936).
8. Mazhukin V.I., Prudkovskii P.A., Samokhin A.A. *Matem. Modelirovanie*, **5**, 3 (1993).
9. Kryukov A.P. *J. Heat Transfer Research*, **24**, 984 (1992).
10. Sone Y., Takata S., Golse F. *Phys. Fluids*, **13**, 324 (2001).
11. Samokhin A.A. *Tr. Inst. Obshchei Fiz. Akad. Nauk SSSR*, **13**, 1 (1990).
12. Mazhukin V.I., Samokhin A.A. *Dokl. Akad. Nauk SSSR*, **281**, 830 (1985).
13. Aden M., Beyer E., Herziger R. *J. Phys. D: Appl. Phys.*, **23**, 655 (1990).
14. Mazhukin V.I., Samarskii A.A. *Serveys on Mathematics for Industry*, **4**, 85 (1994).
15. Mazhukin V.I., Pestryakova G.A. *Dokl. Akad. Nauk SSSR*, **278**, 843 (1984).
16. Mazhukin V.I., Pestryakova G.A. *Zh. Vych. Matem. i Matem. Fiz.*, **25**, 1697 (1985).
17. Breslavskii P.V., Mazhukin V.I. Preprint No. 2 (Moscow: VTsMM RAN, 1992).
18. Jeong S.H., Greif R., Russo R.E. *Appl. Surf. Sci.*, **127–129**, 177 (1998).
19. Gusarov A.V., Smurov I. *Phys. Fluids*, **14**, 4242 (2002).
20. Knight Ch.J. *AIAA J.*, **20**, 950 (1982).
21. Mazhukin V.I., Samokhin A.A. *Kvantovaya Elektron.*, **11**, 2432 (1984) [*Sov. J. Quantum Electron.*, **14**, 1608 (1984)].
22. Bergel'son V.I., Nemchinov I.V. *Kvantovaya Elektron.*, **5**, 2123 (1978) [*Sov. J. Quantum Electron.*, **8**, 1198 (1978)].
23. Phipps C., Dreyfus R., in *Laser Microprobe Mass Analysis*. Ed. by A. Vertes, R. Gijbels, F. Adams (New York: John Wiley & Sons, 1993) p. 2.
24. Vertes A., Dreyfus R.W., Platt D.E. *IBM J. Res. Dev.*, **38**, 1 (1994).
25. Romanov G.S., Stankevich Yu.A. *Fiz. Khim. Obrabot. Mater.*, (4) 15 (1981).
26. Zubov V.I., Krivtsov V.M., Naumova I.N., Shmyglevskii Yu.D. *Zh. Vych. Matem. Matem. Fiz.*, **23**, 1520 (1983).
27. Aden M., Kreutz E.W., Voss A. *J. Phys. D: Appl. Phys.*, **25**, 1545 (1993).
28. Ho J.R., Grogoropoulos C.P., Humphrey J.A.C. *J. Appl. Phys.*, **79**, 7205 (1996).
29. Metev S.M., Veiko V.P. *Laser-Assisted Microtechnology* (Berlin: Springer-Verlag, 1998).
30. Gorbunov A. *Laser-Assisted Synthesis of Nanostructured Materials. Fortschr.-Ber. VDI* (Dusseldorf, VDI Verlag, 2002) Vol. 9, No. 357.
31. Carslaw H.S., Jaeger J.G. *Conduction of Heat in Solids* (Oxford: Clarendon, 1959).
32. Chetverushkin B.N. *Matematicheskoe modelirovanie dinamiki izluchayushchego gaza* (Mathematical Dynamics Simulation of Radiating Gas) (Moscow: Nauka, 1985).
33. Zel'dovich Ya.B., Raizer Yu.P. *Physics of Shock Waves and High-Temperature Hydrodynamic Phenomena* (New York: Academic Press, 1966, 1967) Vols 1 and 2.
34. Kalitkin N.N., Ritus I.V., Mironov A.M. Preprint No. 6 (Moscow: IPM AN SSSR, 1983).
35. Romanov G.S., Stepanov K.L., Syrkin M.I. *Opt. Spektrosk.*, **53**, 642 (1982).
36. Aoki K., Sone Y., Yamada T. *Phys. Fluids A*, **2**, 1867 (1990).
37. Samarskii A.A. *Teoriya raznostnykh skhem* (Theory of Finite-Difference Schemes) (Moscow: Nauka, 1977).
38. Volchinskaya M.I., Mazhukin V.I., Chetverushkin B.N., Churbanova N.G. *Zh. Vych. Matem. i Matem. Fiz.*, **23**, 1177 (1983).
39. Grigor'ev I.S., Meilikhov E.Z. (Eds) *Fizicheskie velichiny. Spravochnik* (Handbook of Physical Quantities) (Moscow: Energoatomizdat, 1991).
40. Rothenberg J.E., Koren G. *Appl. Phys. Lett.*, **44**, 664 (1984).
41. Hermann J., Vivien C., Carricato A.P., Boulmer-Leborgne C. *Appl. Surf. Sci.*, **127–129**, 645 (1998).
42. Gaidarenko D.V., Leonov A.G., Chekhov D.I. *Fiz. Plazmy*, **17** (8), 918 (1991).
43. Ageev V.P., Gorbunov A.A., Konov V.I. *Kvantovaya Elektron.*, **16**, 1214 (1989) [*Sov. J. Quantum Electron.*, **19**, 785 (1989)].
44. Weyl G. *J. Thermophysics and Heat Transfer*, **8**, 229 (1994).